Journal of Geophysical Research: Atmospheres

RESEARCH ARTICLE
10.1029/2018JD028954

Direct Measurements of Dry and Wet Deposition of Black Carbon Over a Grassland

Ethan W. Emerson[1], Joseph M. Katich[2], Joshua P. Schwarz[2], Gavin R. McMeeking[3], and Delphine K. Farmer[1]

[1]Department of Chemistry, Colorado State University, Fort Collins, CO, USA, [2]Chemical Sciences Division, Earth System Research Laboratory, National Oceanic and Atmospheric Administration, Boulder, CO, USA, [3]Handix Scientific Inc., Boulder, CO, USA

Key Points:
- First direct measurements of black carbon by SP2 and eddy covariance over grassland suggest a dry deposition velocity of 0.3 ± 0.2 mm/s
- Wet deposition is the dominant process of black carbon loss, but dry deposition can significantly impact black carbon lifetime
- Measurements suggest that current atmospheric model parameterizations capture the atmospheric lifetime of black carbon reasonably well

Supporting Information:
- Supporting Information S1

Correspondence to:
D. K. Farmer,
delphine.farmer@colostate.edu

Citation:
Emerson, E. W., Katich, J. M., Schwarz, J. P., McMeeking, G. R., & Farmer, D. K. (2018). Direct measurements of dry and wet deposition of black carbon over a grassland. *Journal of Geophysical Research: Atmospheres*, *123*, 12,277–12,290. https://doi.org/10.1029/2018JD028954

Received 7 MAY 2018
Accepted 11 OCT 2018
Accepted article online 21 OCT 2018
Published online 9 NOV 2018

Abstract The atmospheric lifetime of black carbon (BC) is controlled by wet and dry deposition, which are poorly constrained by observations. We show that the single-particle soot photometer can measure surface-atmosphere exchange fluxes of refractory BC (rBC) particle mass (m_{rBC}) and number (N_{rBC}) by eddy covariance. We report field measurements of rBC dry and wet deposition rates during summer 2017 at the Southern Great Plains site in Oklahoma. On average, dry deposition of rBC is 0.3 ± 0.2 mm/s. We estimate a wet deposition flux of 2,600 ng·m^{-2}·hr^{-1} over the 148.5 mm of rainfall observed. These data indicate a composite lifetime of 7–11 days.

1. Introduction

Black carbon (BC) absorbs incident solar radiation, perturbs temperature gradients in the atmosphere, and indirectly impacts cloud formation and optical properties (Koch & Del Genio, 2010). Deposition of BC to snow and ice surfaces alters their albedo and enhances melt (Flanner et al., 2007; Hansen & Nazarenko, 2004). The impact of BC on regional and global climates through these processes depends on its atmospheric concentration and thus on the relative rates of emission and loss. Combustion of fossil fuels and biofuel, biomass burning, and wildfires are major sources of BC (Bond et al., 2004). The only atmospheric sinks for BC aerosol are wet and dry deposition. Wet deposition occurs through scavenging by cloud droplets, ice crystals, and precipitation, while dry deposition refers to the direct removal of particles in the atmosphere to planetary surfaces (e.g., plant, soil, ocean, ice surfaces) by gravitational settling, impaction, interception, and diffusion. The relative importance of these loss processes depends on particle size, with gravitational settling affecting larger (>1 μm in diameter) particles and diffusion impacting the smaller (<300 nm) particles (Ruijrok et al., 1995). Bond et al. (2013) and references therein demonstrate clear constraints on the sources, aging, and optical properties of BC, yet direct constraints on deposition losses are still needed. Removal rates of refractory and nonrefractory submicron aerosol by wet and dry deposition are one of the most uncertain aspects of modeling cloud condensation nuclei (Lee et al., 2013). BC is an ideal tracer for particle deposition because it is nonvolatile and effectively chemically inert, although it becomes internally mixed with other aerosol species in the atmosphere; still, BC is insoluble in water and has no confounding gas-phase contribution to precipitation measurements, enabling its use to examine the relative importance of wet and dry deposition. Thus, measurements of BC deposition are not only essential for constraining BC sinks and atmospheric lifetime but also useful for investigating aerosol deposition more broadly.

The accuracy of BC dry deposition in climate simulations is particularly important in regions with high snow and ice cover due to its albedo impacts. BC deposition to snowpacks is linked to accelerated snowmelt in the Himalaya, Cascades, and Sierra Nevada mountains—thus affecting water supplies for agriculture and population centers (Kaspari et al., 2015; Menon et al., 2010; Yasunari et al., 2013). The current inability of climate researchers to accurately predict BC concentrations in or on snow surfaces, and subsequent impacts on albedo, temperature, and snowmelt, is directly linked to poor parameterizations of BC dry deposition and a lack of deposition measurements. For example, Huang et al. (2010) showed that alterations for dry deposition over the base model is essential to correctly model surface BC concentrations. Furthermore, the use of an unaltered dry deposition simulation underestimated surface BC by a factor of at least 2 and more often >5 (Huang et al., 2010) using the size-resolved resistance-in-series approach developed by Zhang et al. (2001). This dry deposition parameterization has never been tested against BC deposition measurements.

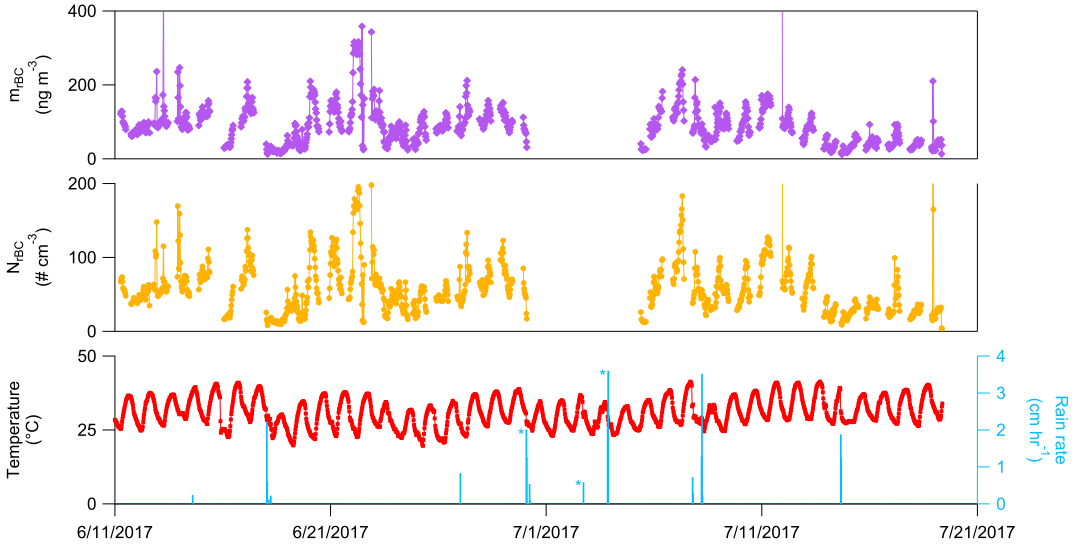

Figure 1. Campaign overview of refractory black carbon (rBC) mass (m_{rBC}), particle counts (N_{rBC}), and meteorological parameters. rBC mass and particle counts represent 30-min averages. Precipitation was collected during rain periods marked with an asterisk (*).

Current methods can quantify wet deposition of BC (e.g., Ohata et al., 2013), but there is a lack of methodology to directly measure dry deposition of BC with adequate time or size resolution to evaluate parameterization schemes. Indirect measurements (Spackman et al., 2010), including those made by collecting particles on artificial surfaces, do not necessarily represent terrestrial surfaces and may not accurately capture surface-atmosphere exchange properties (Dasch & Cadle, 1989; Ogren et al., 1984). Bulk measurement of deposition on snow surfaces approximates dry deposition but lacks the aerosol size resolution to fully evaluate parameterizations. Furthermore, both methods lack sufficient time resolution to capture changes in atmosphere turbulence parameters (e.g., friction velocity), which are key components in dry deposition parameterizations. Micrometeorological techniques show more promise for surface-atmosphere exchange measurements. Here we extend established eddy covariance flux techniques (Lee et al., 2005) by using a single-particle soot photometer (SP2) to measure fluxes of refractory BC (rBC) over a grassland in the United States and compare these exchange measurements with wet deposition collected simultaneously from precipitation.

2. Methods

2.1. Site and Instrumentation

The Black Carbon Aerosol Deposition Study (BCADS) 2017 took place at the Department of Energy Atmospheric Radiation Measurement (ARM) Southern Great Plains (SGP) site in Lamont, Oklahoma, USA (36°36′18″N, 97°29′6″W; 312 m above sea level) from 12 June to 19 July 2017. SGP is a well-known site and has been described elsewhere (Fischer et al., 2007; Riley et al., 2009; Sisterson et al., 2016). The fields to the south and west of the site were planted with alfalfa (*Medicago sativa*), which was swathed 5 and 18 June and grew to a height of 36 cm at the time of the second swathing. Thus, our canopy varied from near 0 to 36 cm over the course of the campaign and had an estimated roughness length of 0.01 to 0.04 m. No direct measurements of leaf area index were collected, but they typically range from 1–5 depending on the crop, season, and year (Fischer et al., 2007).

Figure 1 shows relevant meteorological parameters; temperatures varied between 25 and 35 °C, and the total precipitation recorded during the campaign was 148.5 mm over eight events. A sonic anemometer (Gill Instruments, WindMaster Pro) and an inlet were located 2.7 m above ground level on the SGP ECOR 14 (CO_2 flux) tower. Instruments were housed in a temperature-controlled enclosure at the base of the tower. Despite the temperature control, the enclosure temperature would exceed the threshold for the SP2 and the laser would occasionally shut off during the hottest parts of the day, limiting data collection during these periods. The inlet was aligned downward (45° ± 15° angle) and located below the center of the sonic

anemometer (~40-cm vertical and ~20-cm horizontal displacement). The inlet was 4.5 m of 4.3-mm-inner-diameter stainless steel with a wire mesh screen to exclude insect and debris contamination and insulated from direct sunlight with pipe foam. Bends were minimized to reduce line losses. A bypass pump coupled to a mass flow controller maintained turbulent flow (~12 L/min; Re ≈ 3,000; residence time of 0.3 s). Particle transport losses in the bypass system are estimated to be <5% for the size range measured by the SP2 (70–600 nm), and laminar flow within the internal SP2 tubing was maintained.

2.2. Single-Particle Soot Photometer

rBC was measured with a SP2 (eight-channel, Model D, Droplet Measurement Technologies, Inc., Longmont, CO; Schwarz et al., 2006; Stephens et al., 2003), which measures rBC in individual particles by quantifying the thermal visible radiation they emit after being heated to vaporization by a 1,064-nm continuous intracavity laser beam. rBC, the accepted term for SP2's data products, is experimentally equivalent to elemental carbon at the level of 15% (Kondo et al., 2012; Petzold et al., 2013). The SP2 was calibrated by measuring the instrument response to mobility-selected fullerene soot (Alfa Aesar 40971, Lot W08A039) converted to mass values using effective density data provided by Gysel et al. (2011). We related the W08A039 lot to the previously characterized FS12S011 lot (e.g., Gysel et al., 2011; Laborde et al., 2012; Moteki & Kondo, 2010) using a linear parameterization. The SP2 is extremely sensitive and selective to a single particle's rBC mass (m_{rBC}) but insensitive to particle mixing state and morphology (Cross et al., 2010). High-frequency variability in particle concentrations can be detected by the SP2, allowing for eddy covariance flux calculation (Lee et al., 2005; Burba & Aderson, 2010).

Here we calibrate rBC in the mass range 0.3–50 fg, corresponding to 70- to 600-nm mobility diameter (70- to 380-nm volume equivalent diameter). This covered 95% and 45% of the accumulation mode of m_{rBC} and N_{rBC}, respectively, in this one mode, based on a lognormal fit to the distributions (supporting information Figure S4). Volume equivalent diameters over the 70- to 600-nm range are considered viable. Significant deviation from a lognormal distribution is observed for m_{rBC} below 60 nm, indicating a loss of counting efficiency. Thus, we consider particles above 70 nm to be appropriately quantified for m_{rBC} and infer N_{rBC} based on the number of detection events with the 70- to 600-nm volume equivalent diameter.

We calculate the signal-to-noise ratio (SNR) of m_{rBC} or N_{rBC} collected by the SP2 during a flux period using the following equation:

$$SNR_i = \frac{\mu_i}{\sigma_{i,\mathrm{zero}}} \tag{1}$$

where i is either m_{rBC} or N_{rBC}, μ is the mean concentration during a measurement period, and σ_{zero} is the standard deviation of that signal when air is sampled through a high-efficiency particulate air filter placed at the inlet of the system (system zero). For these data, $SNR_{N_{rBC}} = 60,000$ and $SNR_{m_{rBC}} = 130$.

2.3. Wet Deposition

Three wet deposition samples were collected using an N-Con Systems Company Inc. atmospheric deposition sampler. Rain rates were measured using a weighing bucket precipitation gauge (ARM Climate Research Facility, Weighing Bucket Precipitation Gauge; Atmospheric Radiation Measurement Climate Research Facility, 2011, 2016). Following a rain event, samples were collected in glass vials and stored at 4 °C. Liquid samples were sonicated briefly, which increased measured concentrations by ~50%, and aerosolized with a carefully characterized nebulizer (a CETAC Marin-5, as described in Katich et al., 2017), before sampling the resulting aerosol with an SP2. This technique has been applied to rain, snow, and ice samples (Ohata et al., 2011; Schwarz et al., 2012).

2.4. Eddy Covariance Measurements

The eddy covariance flux technique directly measures a species' surface-atmosphere exchange. The eddy covariance vertical flux (F_c) for a given scalar crossing the measurement plane of a horizontally homogenous area (e.g., prairie grassland) is determined by the covariance of the vertical wind speed (w) and scalar (c; e.g., species mixing ratio or particle concentration; Baldocchi et al., 1988):

$$F_c = \overline{\langle w'c' \rangle} = \frac{1}{n} \sum_{i=0}^{n} (c_i - \overline{c}) \ (w_i - \overline{w}) \tag{2}$$

where n is the number of points used in the calculation; w_i and c_i are instantaneous measurements of vertical wind speed and scalar (e.g., m_{rBC}), respectively; and $\overline{w}$ and $\overline{c}$ are the mean vertical wind speed and scalar measurement, respectively. Eddy covariance flux measurements are typically calculated over 30-min intervals. The exchange velocity (V_{ex}) is determined from the flux and mean concentration over the flux period as follows:

$$V_{ex} = \frac{F_c}{\overline{c}} \tag{3}$$

A negative V_{ex} (or F_c) indicates deposition, and a positive V_{ex} (or F_c) indicates emission. Furthermore, we note that deposition velocity is described by $V_{dep} = -V_{ex}$.

2.4.1. Data Treatment

High-resolution particle-by-particle data are aggregated to a 0.1-s time grid spanning the campaign. Particle number (N_{rBC}) is simply the total count, and particle mass (m_{rBC}) is the sum of masses occurring within 0.05 s before and after the grid point. Concentrations are determined using 1-s averaged flow rates measured by a differential pressure transducer and then converted to standard units using the onboard pressure and temperature measurements. Sonic anemometer data were recorded at 10 Hz on the same computer as rBC data, eliminating the need to adjust digital clocks. These data are gridded to the same particle time grid.

2.4.2. Flux Approach and Calculations

Flux periods are determined based on the flow controller set point changes, which occurred every 30 min throughout the campaign. Preliminary data control excludes periods when laser power changes (typically laser power scans) and times when the measured flow rates vary significantly (3× set point). A total of 905 thirty-minute flux periods are determined to meet data control standards.

Our approach to calculating eddy covariance fluxes of both m_{rBC} and N_{rBC} is outlined below. Further itemized are the quality control filters we employed, corrections, and considerations of corrections. We explicitly note whether a particular correction is applied or not.

1. Calibration of SP2 for particle mass (described above section 2) and correction of vertical wind speed per technical note KN1509v3.
2. Time lag correction: We adjust the data for the time lag between the sonic and SP2 instrument. In our analysis we compared two approaches to time lag correction: (1) a calculated time lag using the flow rate through the inlet tubing (fix or fixed) and (2) using an autocorrelation analysis (max method, not shown; Farmer et al., 2006; Nemitz et al., 2008). Fixed lag times typically underestimate flux measurements because lag times are not always constant (due to variations in pumping speed and changes in air density; Langford et al., 2015). However, autocorrelation analysis of noisy data is limited by counting statistics and can lead to flux overestimation because it systematically maximizes the flux (Langford et al., 2015; Taipale et al., 2010). Data shown here use a fixed lag time of 0.3 s based on tubing length and measured flow rates.
3. Sonic rotation: We apply a two-dimensional rotation to wind speed in three axes to account for the sonic anemometer not being precisely level with the ground and for slope effects in the surrounding area (Lee et al., 2005; Massman, 2000; Wilczak et al., 2001).
4. Flux calculation: See equation (2).

2.4.2.1. Quality Control

We use the following: (1) stationarity test, (2) wind direction, (3) u^*, and (4) precipitation events. Quality filters resulted in $N = 368$ and $N = 236$ flux periods for mass and particle counts, respectively.

1. The stationarity test is applied to meet the requirement that calculated fluxes do not vary within the time scales of analysis and is computed by comparing 5-min fluxes to the overall flux (Foken & Wichura, 1996). During BCADS 2017, we found $N = 514$ stationary periods for m_{rBC} and $N = 326$ for N_{rBC}.

$$0.7 < \frac{\overline{\langle w'c' \rangle}_{5\ min}}{\overline{\langle w'c' \rangle}_{30\ min}} < 1.3 \tag{4}$$

2. Flux periods with an average wind direction that is obstructed by the sampling tower or passes through the SGP ARM site are excluded ($N = 38$).

3. Periods with low friction velocity ($u^* < 0.15$ m/s; $N = 243$) are excluded (Papale et al., 2006).
4. Precipitation events (eight in total; impacting $N = 5$ flux periods) are excluded from the general analysis, but fluxes during periods of rain are considered and discussed.

2.4.2.2. Corrections

We consider the following corrections that can be applied to eddy covariance particle data: (1) storage, (2) time response, (3) sensor separation, (4) tube attenuation, (5) Webb-Pearman-Leuning, (6) despiking, and (7) detrending. The storage correction is found to be significant and is thus included in our analysis. All remaining corrections are neglected from the presented data, but we note the magnitude of error these could contribute.

1. Under horizontally homogenous conditions, the turbulent flux below the measurement height can differ. We use a 1-point storage term developed by Rannik et al. (2009):

$$F_{\text{storage}} = \int_0^{z_r} \frac{\partial \overline{c}}{\partial t} dz \approx z_r \frac{\overline{c(t+\Delta T)} - \overline{c(t)}}{\Delta T} \tag{5}$$

   where c is the concentration and $t = 2$ min with $\Delta T = 30$ min. These values were calculated for all flux periods that ended within 10 s of the next one starting ($N = 862$). We estimate the storage contribution for m_{rBC} and N_{rBC} to be 15% and 30%, respectively, on average. This correction is included in our analysis.
2. Time response corrections are necessary to compensate for insufficient sensor response time (Lee et al., 2005; Massman, 2000; Moore, 1986). This correction is neglected as the SP2 measures on a particle-by-particle basis and within the calibrated range the SP2 has a counting efficiency near 100%. Errors associated with missed particles are expected to be random, and thus, no explicit correction is included.
3. Sensor separation corrections are used to correct for the inability of most closed-path systems that draw from an inlet to sample from the same volume as vertical wind speed. Using formulations developed by Kristensen et al. (1997), we estimate the losses to be <5%. As evidenced in Figure 3, high-frequency losses are not observed and thus not corrected.
4. Tube attenuation corrects for flux losses within the inlet that dampens small fluctuations. Spectral analysis (see below) show that attenuation does not occur substantially at high frequencies, and thus, we neglect this correction. However, due to the noisy nature of cospectra with noisy scalars and limited counting statistics, attenuation could be 5–10%.
5. Webb-Pearman-Leuning correction is neglected as flow rates through the system are measured in volume but converted to standard units using high-speed onboard measurements of temperature and pressure.
6. Despiking is neglected because a small number of particles are sampled over 100 ms and are also not necessarily continuous; thus, particle flux measurements are usually limited by counting statistics (Nemitz et al., 2008; Pryor, Gallagler, et al., 2008). Furthermore, particle size impacts the flux measurement as larger particles carry the bulk of the particle mass but are limited in number. Nemitz et al. (2008) describe how these large particles appear as spikes in 100-ms resolution time series and contribute a real flux and should not be removed by a despiking routine.
7. No detrending method is applied to this data set because detrending techniques typically result in a loss of flux and are usually required for situations where the meteorology is changing rapidly (Moncrieff et al., 2004). Periods of distinct meteorology (rain events) and nonstationary flux periods are already removed, and this correction would be minimal.

2.5. Flux Uncertainty

We examine two sources of uncertainty affecting our flux measurements and report data for only flux periods meeting quality control metrics. Uncertainty can be associated with counting discrete particles (N_{rBC}), measurement of particle mass (m_{rBC}), instrument noise, and the measurement of covariance. Flux uncertainty $\Delta F_{N_{\text{rBC}}}$ caused by counting statistics for a single 30-min period is expressed as follows:

$$\Delta F_{N_{\text{rBC}}} = \frac{\sigma_w \overline{c}}{\sqrt{N}} \tag{6}$$

where N is the cumulative number of particles counted in the 30-min period (Fairall, 1984; Nemitz et al., 2008). For these data, $\Delta F_{N_{\text{rBC}}} = 0.02$ #·cm^{-2}·s^{-1}.

Table 1
Uncertainty and LOD Metrics for the 2017 BCADS Campaign

Identifier	*SNR*	$\Delta F_{N_{rBC}}$	δF_{noise}	σ_f	$\overline{LOD}_F$	Beyond $\overline{LOD}_F$	$\overline{LOD}_{V_{ex}}$	Beyond $\overline{LOD}_{V_{ex}}$
Units	a.u.	[ng or #]·[m^{-2} or cm^{-2}]·s^{-1}				#	mm^{-2}·s^{-1}	#
m_{rBC}	130	n/a	0.2	0.02	0.04	342/368	0.6	353/368
N_{rBC}	60,000	0.02	0.05	0.06	0.01	202/236	0.2	217/236

Note. All flux data are in units of ng·m^{-2}·s^{-1} and #·cm^{-2}·s^{-1} for m_{rBC} and N_{rBC}, respectively. Units for all other data are specified.

Various methods exist that quantify the uncertainty of covariance between vertical wind speed and scalar (e.g., Finkelstein & Sims, 2001; Lenschow & Kristensen, 1985; Mahrt, 1998; Wienhold, 1995; Wyngaard, 1973), and we find them to be comparable for these data. We report the random flux errors using properties of the cross-covariance function of a single-flux measurement from the baseline fluctuation (standard deviation; $\sigma_{f(w'c')}$) in a cross-covariance function (f) between vertical wind speed (w) and scalar (c) at lag times significantly longer than the delay time ($\pm\Gamma$, where Γ = 30 to 60 s; Spirig et al., 2005; Wienhold, 1995). We calculate the detection limit of a single-flux measurement (LOD_σ) as $3 \times \sigma_{f(w'c')\ [-\Gamma,+\Gamma]}$ (Langford et al., 2015). For these data, $\sigma_{f\left(w'N'_{rBC}\right)} = 0.05$ #·cm^{-2}·s^{-1} and $\sigma_{f\left(w'm'_{rBC}\right)} = 0.24$ ng·m^{-2}·s^{-1}.

We further estimate the flux uncertainty due to instrument noise δF_{noise} as described by Billesbach (2011):

$$\delta F_{noise} = \frac{1}{M}\sum_{j,k=1}^{M} w'(t_j)c'(t_k) \tag{7}$$

where w' and c' are deviations from the mean of vertical wind speed (w) and scalar (c) normalized by the number of measurements (M) within the averaging interval and the time indices j and k, where k is the index of the randomized time series. For these data, $\delta F_{N_{rBC},noise} = 0.04$ #·cm^{-2}·s^{-1} and $\delta F_{m_{rBC},noise} = 0.2$ ng·m^{-2}·s^{-1}.

2.6. Flux Limit of Detection

We determine a limit of detection of a given flux period (LOD_i) as described by Langford et al. (2015):

$$LOD_i = \alpha * RE_i \tag{8}$$

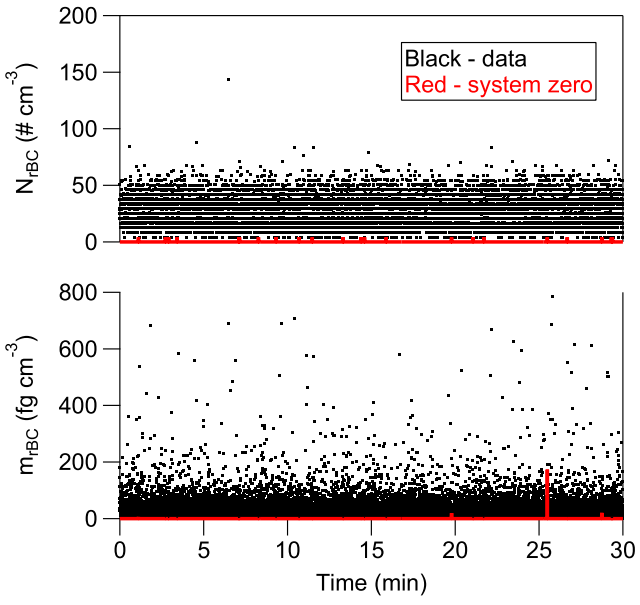

Figure 2. An example of 30-min high time resolution m_{rBC} and N_{rBC} particle data (black) with 30-min system zero data from the adjacent half-hour.

where α is a specified confidence interval (α = 3 for the 99th percentile) and RE_i is the random error for the flux period (described above). We aggregate the LOD_i data (of quality-controlled data) to determine an average campaign limit of detection ($\overline{LOD}$).

$$\overline{LOD} = \frac{1}{N}\sqrt{\Sigma_{i=1}^{N} LOD_i^2} \tag{9}$$

Averaged over the entire field project, $\overline{LOD}_{N_{rBC},\ F} = 0.01$ #·cm^{-2}·s^{-1} and $\overline{LOD}_{m_{rBC},F} = 0.04$ ng·m^{-2}·s^{-1}. The same method was applied to determine a V_{ex} limit of detection $\overline{LOD}_{N_{rBC},\ V_{ex}} = 0.2$ mm^{-2}·s^{-1} and $\overline{LOD}_{m_{rBC},\ V_{ex}} = 0.6$ mm^{-2}·s^{-1}. On a per-flux-period basis, the flux was beyond σ_f (uncertainty) N = 171/368 and N = 117/236 instances for m_{rBC} and N_{rBC}, respectively. The number of flux periods exceeding the campaign $\overline{LOD}$ is N = 342/368 for m_{rBC} and N = 202/236 for N_{rBC}. See Table 1.

2.7. Wet Deposition Flux

The rBC concentration of the three collected rain events is determined and based on the rainfall during the event. A wet deposition flux is determined following Mori et al. (2014). For each event, the concentration of rBC $C_{rBCprecip}$ is determined in ng_{rBC}/g_{H2O}. This mass loading is scaled by the

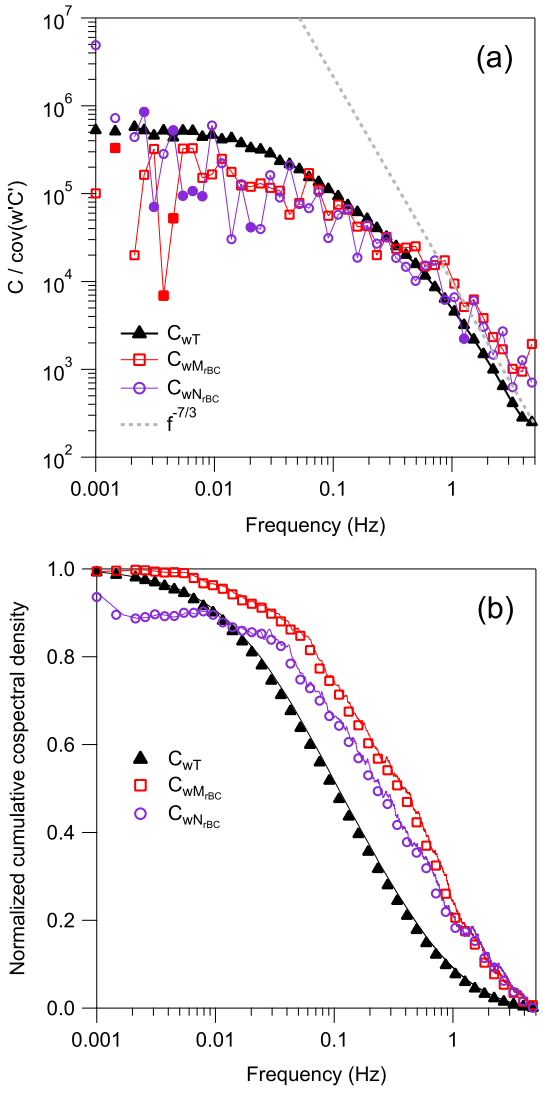

Figure 3. (a) Covariance normalized cospectral density of m_{rBC} (red squares) N_{rBC} (purple circles) and temperature (black closed triangles). For (a), m_{rBC} and N_{rBC} open symbols indicate positive values, and closed symbols indicate negative values flipped positive. Data represent ensemble medians of quality-controlled flux periods binned into 35 evenly spaced logarithmic bins. Any negative values are shown as positive after all manipulations. (b) Cumulative cospectral density plot for data presented in (a).

amount of precipitation collected (P_e) in the event (mm) to calculate the flux per event (ng·m^{-2}·event^{-1}).

$$F_{rBC\,precip} = C_{rBC\,precip} \times P_e \quad (10)$$

Each event flux is weighted by R, the fractional contribution of the measured rain (in the event) to the total rain during the campaign (= P_e/P_{total}). An average flux is derived by averaging the weighted event flux of the three rain events by the campaign duration (hr; details in Table S1). This method effectively represents the flux if each rain event represented the entire campaign. The Mori et al. (2014) method results in a value that is within the standard deviation of the three rain events.

3. Method Validation

To demonstrate the ability of the SP2 to measure m_{rBC} and N_{rBC} fluxes, we use three approaches: (1) spectral analysis to demonstrate that the SP2 meets the instrumental requirements for eddy covariance flux measurements; (2) quantitative constraints on uncertainty and detection limits; and (3) internal comparison of m_{rBC} and N_{rBC} fluxes.

3.1. Instrument Response Time

As described previously, instruments used for eddy covariance flux analysis must be both fast and sensitive on the time scale of turbulent eddies. Figure 2 shows a signal that is clearly distinguishable over the system background. System background is determined by a 30-min period where air is drawn through a high-efficiency particulate air filter placed at the inlet of the entire system. As mentioned previously, the average SNR for m_{rBC} and N_{rBC} is more than 100. Concentrations have a strong diel trend but did not typically vary significantly over the course of 30 min. However, an instrument with a good SNR is not necessarily inherently suitable for eddy covariance flux analysis.

3.2. Spectral Analysis

The eddy covariance method requires sufficiently fast sensor response, adequate integration time, and sensitive measurements. These requirements are validated by spectral analysis (Figure 3), in which the cospectra of vertical wind speed and rBC measurement (m_{rBC} or N_{rBC}) are compared to the simultaneously measured sensible heat flux. Ensemble flux data for quality-controlled data show a $(f)^{-7/3}$ response between 0.3 and 3 Hz, characteristic of the inertial subrange predicted from the Kolmogorov theory (Kaimal & Finnigan, 1994) and demonstrates a sufficiently fast sensor response time to measure eddy covariance fluxes (Baldocchi et al., 1988). Both m_{rBC} and N_{rBC} follow the sensible heat cospectrum, implying that scalar transport occurs by the energy-transporting eddies. The lack of spectral attenuation (i.e., steeper slope at high frequencies) indicates no flux underestimation due to high-frequency damping within inlet lines and that the instrument has a sufficiently fast response for eddy covariance flux measurements.

Unscaled cumulative cospectra (Figure 3b) show which frequencies contribute to the total flux and demonstrate sufficiently long integration times. At low frequencies, cumulative cospectra for all measured scalars are near unity, implying a sufficiently long integration time. We attempted to calculate spectral losses empirically by comparing N_{rBC} and m_{rBC} to the reference (sensible heat) cospectra, but the cospectral shapes are not suitable to quantify losses. This is likely due to uncertainty and the noisy cospectral

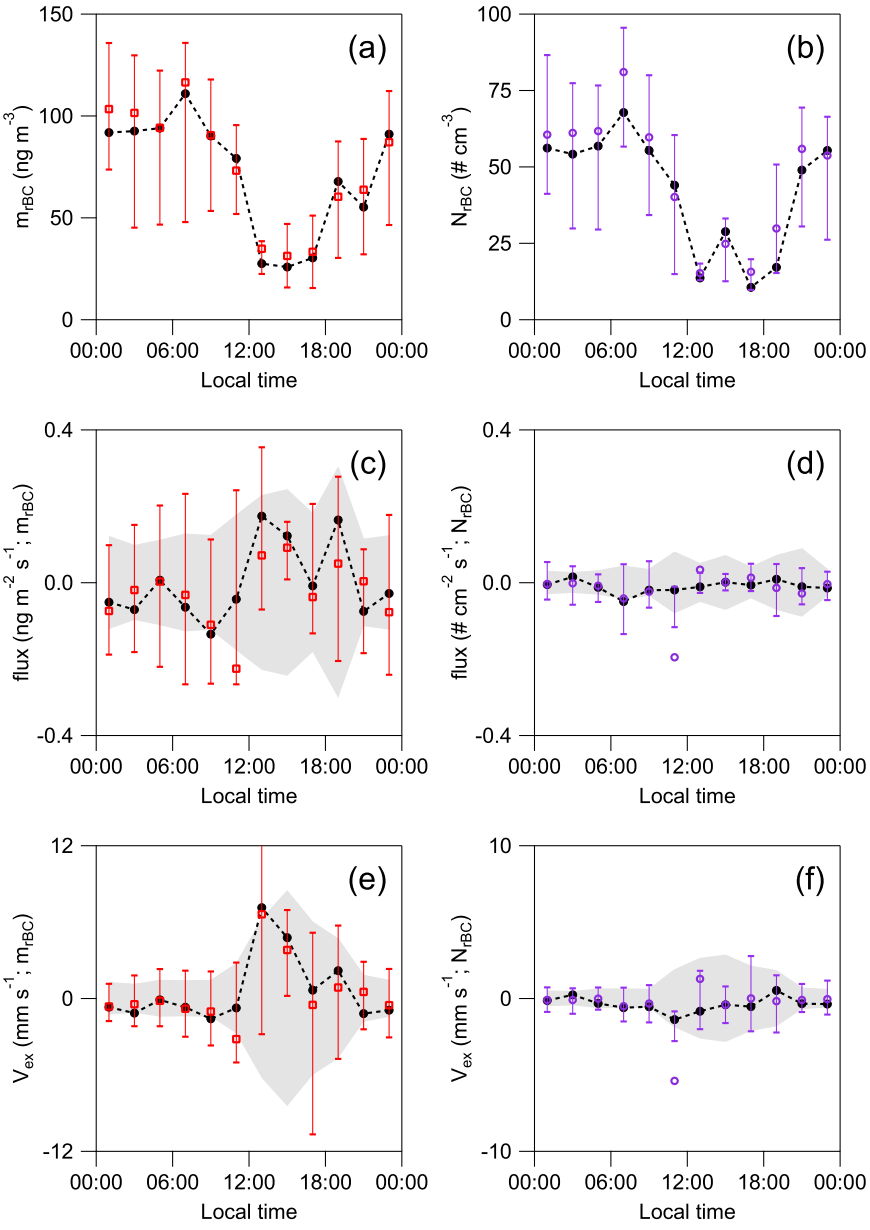

Figure 4. Bihourly binned data of (left) m_{rBC} and (right) N_{rBC}. Plots of (top) concentration, (middle) flux, and (bottom) V_{ex}. Open symbols are averages for the bin, and closed symbols with dashed lines connecting are medians. The whiskers denote the 25th and 75th percentiles. The shaded gray denotes a bihourly average limit of detection (calculation described in section 2).

data, which are especially present at high frequencies. Both m_{rBC} and N_{rBC} trend with sensible heat but do not flatten at the highest frequencies.

3.3. Quantitative Constraints on Uncertainty and Detection Limits

Various sources contribute to uncertainty for particle eddy covariance measurements. The number of particles sampled in 100 ms is typically small; as such, particle measurements are typically limited by counting statistics (Nemitz et al., 2008; Pryor, Larsen, et al., 2008). Additionally, particle size impacts the uncertainty as larger particles carry most of the measured mass (Jimenez, 2003). Despiking routines are typically omitted due to the inherent noise observed in particle measurements. As mentioned above, we employed a method developed by Wienhold (1995) to determine the uncertainty of a flux

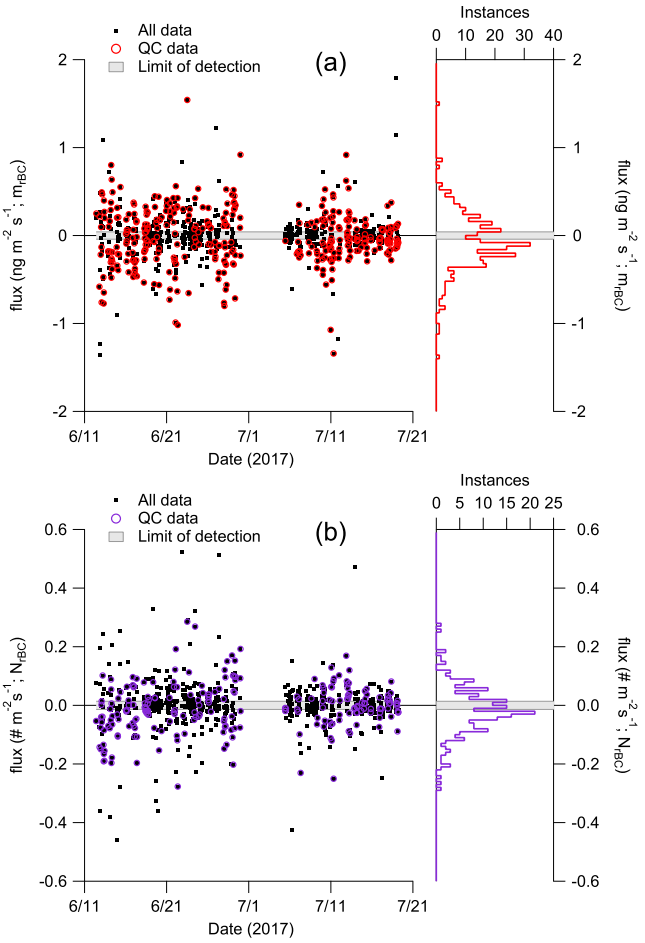

Figure 5. Campaign time series of (a) m_{rBC} and (b) N_{rBC} fluxes for all data (solid symbols) and quality-controlled data (open symbols); uncertainty associated with each measurement is omitted for clarity. Binned data are shown on the right for each plot with the overall campaign average shown in gray across the entire time series.

measurement from baseline fluctuations at time lags significantly longer than the prescribed lag time. The uncertainty for neither m_{rBC} nor N_{rBC} fluxes is constant across the campaign and increases quadratically with the flux magnitude. Furthermore, these errors follow a power law relationship with higher friction velocity and are consistent with previous observations (Farmer et al., 2011) and theoretical considerations showing that concentration measurement precision must be higher during more turbulent conditions (Fairall, 1984; Rowe et al., 2011). These behaviors suggest increased mixing or inefficient scavenging by terrestrial surfaces. Because of these observations, it is necessary to consider ensemble averages for scientific interpretation. Specifically, we interpret data that are beyond the $\overline{LOD_F}$ or $\overline{LOD_{V_{ex}}}$ despite the fact that the singular data may not be above the LOD_i for that specific data point (i.e., the uncertainty for that *i*th point includes zero).

3.4. Internal Comparisons

Fluxes of m_{rBC} and N_{rBC} are not always consistent and bifurcate (i.e., m_{rBC} and N_{rBC} fluxes in opposite directions) 18% of the time. The remaining 82% behave consistently. No statistically significant trend between deviating fluxes and any measured external parameter (i.e., wind direction, u^*, and rBC concentration). Upward particle fluxes are not an uncommon observation (e.g., Pryor, Barthelmie, et al., 2008); however, bifurcated fluxes of particle counts versus particle mass are unusual. Quadrant analysis indicates that different micrometerological events coupled with changes in particle concentrations lead to apparent upward fluxes. Bifurcated fluxes are more surprising and indicate that processes controlling particle mass and particle number fluxes can be decoupled. For example, a gradient with smaller particles near the ground than above the sensor, but fewer larger particles near the ground than above the sensor, could cause an apparent upward flux in particle number and an apparent downward flux in particle mass. In contrast, consistent m_{rBC} and N_{rBC} fluxes indicate that both small and large particles have consistent vertical gradients. An eddy can thus carry m_{rBC} fluxes upward while having a downward N_{rBC} flux.

4. Observations and Discussion

4.1. rBC Fluxes

Concentrations of m_{rBC} and N_{rBC} (Figure 1) are representative of a remote North American field site away from major anthropogenic influences (Koch et al., 2009). During BCADS 2017 the geometric mean (μ_g) with a geometric standard deviation (σ_g) for m_{rBC} and N_{rBC} concentrations are μ_g = 56 (σ_g = 3.0) ng·sm^{-3} and μ_g = 46 (σ_g = 2.2) #·sccm^{-3}. These concentrations follow a diel cycle (Figure 4) consistent with regular boundary layer expansion observed at the site (Figure S5). m_{rBC} and N_{rBC} concentrations had a consistent daily range throughout the campaign until the last week (11 to 19 July), when concentrations decreased.

Complete campaign data of m_{rBC} and N_{rBC} fluxes are shown in Figure 5. Variability in these data is clearly observed. While the magnitude of a single-flux measurement rarely exceeds the LOD_i, it frequently exceeds the single-flux point uncertainty (σ_f); we include all data that meet the filtering criteria in the analysis to accurately derive the aggregate statistics. The histogram in Figure 5 shows the propensity for deposition occurring at the field site. No daily trends associated with emission could be discerned. Moreover, as there are no direct sources within the flux footprint, observations should represent loss processes only. However, as noted above, upward fluxes are observed and occur around noon. While boundary layer height does not drive fluxes, in-mixing of lower loadings from the free

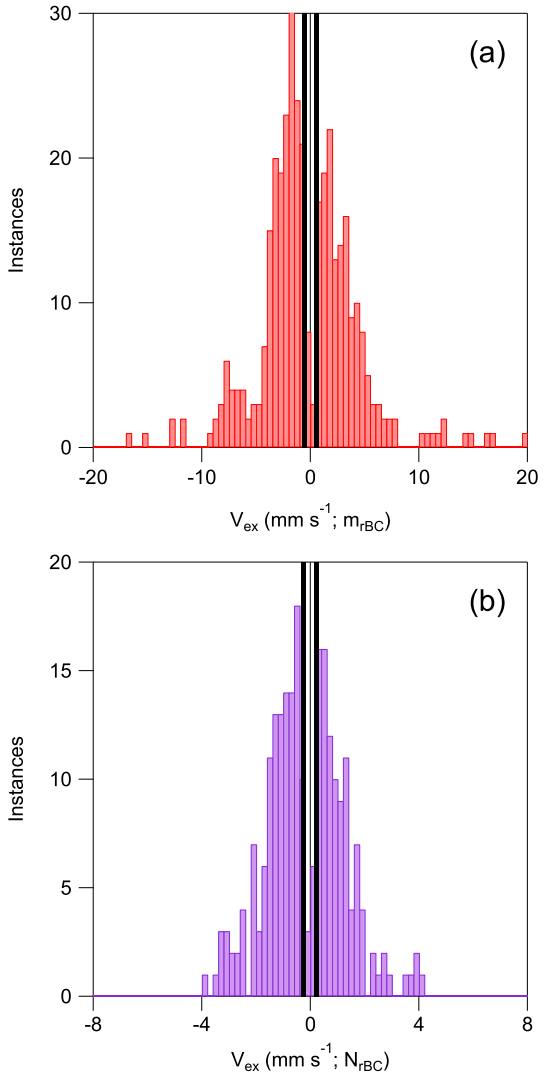

Figure 6. Histogram of (a) m_{rBC} and (b) N_{rBC} V_{ex} in mm/s. The limits of detection are shown as thick black lines.

troposphere could create an apparent upward flux. Thus, a flux period in which downdrafts containing particle-depleted air (i.e., entrainment processes) would have an upward flux. Such effects have been noticed for particle fluxes (Nilsson et al., 2016; Pryor, Barthelmie, et al., 2008). Enhanced downward fluxes in the midafternoon are likely a result of increased atmospheric turbulence and friction velocity (Figure S6). V_{dep} tends to increase with u^*, but the correlation is inadequate to establish a parameterization ($r^2 \approx 0.2$ for both mass and counts). Nighttime fluxes tend to be downward and relatively small; this suggests that particle settling through the more stagnant nocturnal boundary layers is occurring. Because these measurements approach the limit of detection for eddy covariance flux analysis, the analysis is very sensitive to minor changes in concentration that are associated with boundary layer dynamics.

The net flux and thus exchange velocity for m_{rBC} and N_{rBC} are near zero; -0.3 ± 0.2 and -0.3 ± 0.2 mm/s for m_{rBC} and N_{rBC}, respectively (including both upward and downward fluxes; uncertainty is from standard deviation). For the average horizontal wind speed and rBC particle diameter at SGP, the implied net deposition is slower than size-resolved parameterizations developed by Zhang et al. (2001), but it is consistent with Wesely (1989) and more recent Arctic BC simulations with deposition velocities of 0.1 to 0.7 mm/s (Liu et al., 2011). These values imply a longer lifetime with respect to dry deposition than current understanding. It is possible that a different process is causing the apparent upward fluxes for rBC, as no known sources exist within the footprint sectors. If the analysis is biased to exclude upward fluxes, V_{dep} is 3.5 ± 0.3 mm/s (m_{rBC}) and 1.6 ± 0.3 mm/s (N_{rBC}), which are consistent Zhang et al. (2001). Lacking a physical explanation for upward fluxes, we cannot reasonably exclude them, and our measurements indicate a longer lifetime of BC with respect to dry deposition. Figure 5 shows the diel trends of concentration, flux, and V_{ex}. Bidirectional exchange occurs throughout the day, but downward fluxes tend to occur in the early morning hours with upward fluxes occurring in the afternoon and slowly subsiding. Deposition is more pronounced in the early morning hour for m_{rBC} and N_{rBC}.

Two distinct modes are apparent in the histogram of V_{ex} and imply a loss process (deposition) and emission process (Figure 6). The observable dip at zero exchange velocity further suggests that despite being near the limit of detection, these fluxes are real and not simply noise. This dip near zero has also been associated with the use of a maximum covariance lag time determination method, but that is not the case here (Langford et al., 2015). Deposition of N_{rBC} is a tighter distribution than that of m_{rBC}, and this discrepancy suggests that particles of different masses deposit and different rates. This observation is consistent with larger particles carrying the bulk of the total measured mass.

4.2. Wet and Dry rBC Deposition

Eight major precipitation events were observed during BCADS 2017 totaling 148.5 mm of rain (ARM Climate Research Facility, Weighing Bucket Precipitation Gauge). This period was climatologically representative of historical averages for June and July in this region. It is expected that rBC washout occurs during or immediately following a rain event. However, only three precipitation events (of six with corresponding SP2 data) show a decrease of ambient N_{rBC} and m_{rBC} concentrations. Below-cloud washout of rBC may not be efficient, and the loss mechanism may be dominated by in-cloud scavenging. This further implies that rBC measured in precipitation is not necessarily representative of ambient rBC concentrations, as in-cloud scavenging could occur far from the measurement site. From three rain events (marked with an asterisk in Figure 2), we estimate a campaign average wet deposition flux ($\bar{F}$) of 0.05 ± 0.02 mg·m^{-2}·day^{-1}.

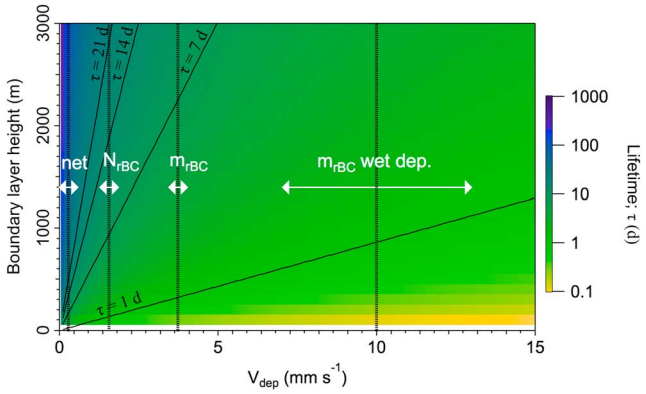

Figure 7. Comparison of refractory black carbon (rBC) lifetimes for dry deposition (by mass and particle counts) and wet deposition as a function of boundary layer height and observed V_{dep}. Both N_{rBC} and m_{rBC} are averages for when only deposition is occurring (i.e., negative flux periods). The net vertical line represents the campaign average V_{dep} (i.e., both negative and positive flux periods for N_{rBC} and m_{rBC}). We note that wet V_{dep} are not true velocities but an expression of scavenging efficiency observed during the Black Carbon Aerosol Deposition Study. White arrows indicate the V_{dep} range, and the vertical offset is the typical boundary layer height observed at Southern Great Plains.

Considering all quality-controlled flux periods, wet deposition dominates the overall m_{rBC} flux and we find that dry deposition constitutes 6% ± 4% of total deposition. These values are on the low end of the typical 5–20% assumed in global climate models (Koch et al., 2009). As mentioned previously, upward fluxes may be either a measurement artifact or real and driven by a different process (e.g., vertical gradients in size distributions). These values are highly dependent on precipitation rates and amount. This also assumes that dry deposition is a loss process from the same air mass. If particles are scavenged by cloud droplets in the free troposphere, the rBC particles observed in precipitation may differ from those in the boundary layer.

Deposition velocities describe the efficiency of the loss process and allow us to estimate the lifetime of rBC with respect to wet and dry deposition (Figure 7). We approximate lifetimes as the time it takes a particle to deposit from the top of the boundary layer. The wet deposition velocity (10 ± 3 mm/s) represents a loss efficiency of rBC and assumes that the rate of loss is invariant with position within the boundary layer and other factors that influence where and the process of loss. For the net flux observed we find a much longer lifetime of 30–90 days for dry deposition for m_{rBC} and N_{rBC}, with a shorter wet deposition lifetime of 1–3 days. A simple wet-versus-dry weighted lifetime suggests a net lifetime of 7-11 days. Which are in the range of the composite 5-11 days typically described in the literature (Koch et al., 2009). In areas where precipitation is limited, the BC lifetime could be significantly longer. While dry deposition rates are assumed to be invariant, wet deposition processes may be first order with respect to rBC burden.

5. Conclusion

The relative importance of wet-versus-dry deposition depends on the amount of precipitation at a given site location and atmospheric burden. While wet deposition controls rBC lifetime, dry deposition can significantly extend the lifetime of rBC in the absence of precipitation. Furthermore, the analysis assumes that wet deposition occurs throughout the boundary layer and could vary if in-cloud scavenging dominates over below-cloud impaction. In regions or time periods of limited precipitation, the relative importance of dry deposition to aerosol lifetime will be higher.

Observed deposition velocities (0.3 ± 0.2 mm/s m_{rBC} and N_{rBC}) are consistent with some current global model approaches and, to our knowledge, represent the first in situ measurements of rBC deposition velocities. However, we acknowledge that these observations were made at a single site over a short timeframe, and the role of surface properties, precipitation, and mass loading on V_{dep} warrants further investigation. Huang et al. (2010) and Reddy and Boucher (2004) employed a global annual mean BC and organic aerosol deposition velocity of 1 mm/s for particle numbers in the submicron mode. Wesely (1989) used a particle number deposition velocity of 0.8 mm/s over snow and ice surfaces, and Liu et al. (2011) improved their Arctic BC simulations with number deposition velocities of 0.1 to 0.7 mm/s. The discrepancy in values used

in cryosphere/Arctic simulations may be due to surface properties, suggesting a need for further rBC flux measurements over the cryosphere and other terrestrial or hydrological surfaces.

Additionally, these measurements represent total particle number for particles with diameter 70–600 nm. However, several widely used particle deposition parameterizations are size dependent, requiring size-resolved fluxes for constraint. In sufficient signal-to-noise environments, size-resolved measurements with the SP2 should be possible as these data show the SP2 to be adequately fast and sensitive enough for eddy covariance flux analysis of m_{rBC} and N_{rBC}. While the total m_{rBC} and N_{rBC} flux is unaffected by internal mixing, size-resolved measurements will require considering particle coating thickness. On the time scale of turbulent eddies (<30 min), m_{rBC} will be unaffected by atmospheric chemistry, but coating thickness may vary due to gas-particle partitioning and in-canopy oxidation and would impact the particle deposition rate. Size-resolved measurements will improve climate model parameterizations, but this study suggests that current models capture BC lifetimes and deposition rates reasonably well.

Acknowledgments
We thank the staff at the Southern Great Plains Atmospheric and Radiation Measurement site including John Schatz, Chris Martin, Ken Teske, and Mark Smith. We also thank the DOE Office of Biological and Environmental Research for funding (grant DE-SC0016259). We would also like to thank the two anonymous reviewers whose thoughts and questions helped bring clarity to this paper. Data collected during this campaign and presented herein are available at https://www.arm.gov/research/campaigns/sgp2017bcads, and select the "Browse Data" button. Alternatively, the following direct link can be used: https://www.archive.arm.gov/discovery/#v/results/s/fiop::sgp2017bcads.

References

Atmospheric Radiation Measurement (ARM) Climate Research Facility (2011). updated hourly. Ceilometer (CEILPBLHT). 2017-06-01 to 2017-07-30, Southern Great Plains (SGP) Central Facility, Lamont, OK (C1). Compiled by B. Ermold and V. Morris. Atmospheric Radiation Measurement (ARM) Climate Research Facility Data Archive: Oak Ridge, Tennessee, USA. Data set accessed 2017-09-20 at https://doi.org/10.5439/1095593

Atmospheric Radiation Measurement (ARM) Climate Research Facility (2016). updated hourly. Weighing Bucket Precipitation Gauge (WBPLUVIO2). 2017-06-01 to 2017-07-31, Southern Great Plains (SGP) Central Facility, Lamont, OK (C1). Compiled by E. Cromwell, J. Delamere and M. Bartholomew. Atmospheric Radiation Measurement (ARM) Climate Research Facility Data Archive: Oak Ridge, Tennessee, USA. Data set accessed 2017-12-08.

Baldocchi, D. D., Hincks, B. B., & Meyers, T. P. (1988). Measuring biosphere-atmosphere exchanges of biologically related gases with micrometeorological methods. *Ecology*, *69*(5), 1331–1340. https://doi.org/10.2307/1941631

Billesbach, D. P. (2011). Estimating uncertainties in individual eddy covariance flux measurements: A comparison of methods and a proposed new method. *Agricultural and Forest Meteorology*, *151*(3), 394–405. https://doi.org/10.1016/j.agrformet.2010.12.001

Bond, T. C., Doherty, S. J., Fahey, D. W., Forster, P. M., Berntsen, T., DeAngelo, B. J., Flanner, M. G., et al. (2013). Bounding the role of black carbon in the climate system: A scientific assessment. *Journal of Geophysical Research: Atmospheres*, *118*, 5380–5552. https://doi.org/10.1002/jgrd.50171

Bond, T. C., Streets, D. G., Yarber, K. F., Nelson, S. M., Woo, J. H., & Klimont, Z. (2004). A technology-based global inventory of black and organic carbon emissions from combustion. *Journal of Geophysical Research*, *109*, D14203. https://doi.org/10.1029/2003JD003697

Burba, G., & Aderson, D. (2010). *A brief practical guide to eddy covariance flux measurements: Principles and workflow examples for scientific and industrial applications*. Lincoln, Nebraska, United States: LI-COR Biosciences.

Cross, E. S., Onasch, T. B., Ahern, A., Wrobel, W., Slowik, J. G., Olfert, J., Lack, D. A., et al. (2010). Soot particle studies−instrument inter-comparison—Project overview. *Aerosol Science and Technology*, *44*(8), 592–611. https://doi.org/10.1080/02786826.2010.482113

Dasch, J. M., & Cadle, S. H. (1989). Atmospheric carbon particles in the Detroit urban area: Wintertime sources and sinks. *Aerosol Science and Technology*, *10*(2), 236–248. https://doi.org/10.1080/02786828908600508

Fairall, C. (1984). Interpretation of eddy-correlation measurements of particulate deposition and aerosol flux. *Atmospheric Environment*, *18*(7), 1329–1337. https://doi.org/10.1016/0004-6981(84)90041-6

Farmer, D. K., Kimmel, J. R., Phillips, G., Docherty, K. S., Worsnop, D. R., Sueper, D., Nemitz, E., et al. (2011). Eddy covariance measurements with high-resolution time-of-flight aerosol mass spectrometry: A new approach to chemically resolved aerosol fluxes. *Atmospheric Measurement Techniques*, *4*(6), 1275–1289. https://doi.org/10.5194/amt-4-1275-2011

Farmer, D. K., Wooldridge, P. J., & Cohen, R. C. (2006). Application of thermal-dissociation laser induced fluorescence (TD-LIF) to measurement of HNO_3, Σalkyl nitrates, Σperoxy nitrates, and NO_2 fluxes using eddy covariance. *Atmospheric Chemistry and Physics*, *6*(11), 3471–3486. https://doi.org/10.5194/acp-6-3471-2006

Finkelstein, P. L., & Sims, P. F. (2001). Sampling error in eddy correlation flux measurements. *Journal of Geophysical Research*, *106*(D4), 3503–3509. https://doi.org/10.1029/2000JD900731

Fischer, M. L., Billesbach, D. P., Berry, J. A., Riley, W. J., & Torn, M. S. (2007). Spatiotemporal variations in growing season exchanges of CO_2, H_2O, and sensible heat in agricultural fields of the Southern Great Plains. *Earth Interactions*, *11*(17), 1–21. https://doi.org/10.1175/EI231.1

Flanner, M. G., Zender, C. S., Randerson, J. T., & Rasch, P. J. (2007). Present-day climate forcing and response from black carbon in snow. *Journal of Geophysical Research*, *112*, D11202. https://doi.org/10.1029/2006JD008003

Foken, T., & Wichura, B. (1996). Tools for quality assessment of surface-based flux measurements. *Agricultural and Forest Meteorology*, *78*(1–2), 83–105. https://doi.org/10.1016/0168-1923(95)02248-1

Gysel, M., Laborde, M., Olfert, J. S., Subramanian, R., & Gréhn, A. J. (2011). Effective density of Aquadag and fullerene soot black carbon reference materials used for SP2 calibration. *Atmospheric Measurement Techniques*, *4*(12), 2851–2858. https://doi.org/10.5194/amt-4-2851-2011

Hansen, J., & Nazarenko, L. (2004). Soot climate forcing via snow and ice albedos. *Proceedings of the National Academy of Sciences*, *101*(2), 423–428. https://doi.org/10.1073/pnas.2237157100

Huang, L., Gong, S. L., Jia, C. Q., & Lavoué, D. (2010). Importance of deposition processes in simulating the seasonality of the Arctic black carbon aerosol. *Journal of Geophysical Research*, *115*, D17207. https://doi.org/10.1029/2009JD013478

Jimenez, J. L. (2003). Ambient aerosol sampling using the Aerodyne aerosol mass spectrometer. *Journal of Geophysical Research*, *108*(D7), 8425. https://doi.org/10.1029/2001JD001213

Kaimal, J. C., & Finnigan, J. J. (1994). *Atmospheric boundary layer flows: Their structure and measurement*. New York Oxford: Oxford university press.

Kaspari, S., McKenzie Skiles, S., Delaney, I., Dixon, D., & Painter, T. H. (2015). Accelerated glacier melt on Snow Dome, Mount Olympus, Washington, USA, due to deposition of black carbon and mineral dust from wildfire. *Journal of Geophysical Research: Atmospheres*, *120*, 2793–2807. https://doi.org/10.1002/2014JD022676

Katich, J. M., Perring, A. E., & Schwarz, J. P. (2017). Optimized detection of particulates from liquid samples in the aerosol phase: Focus on black carbon. *Aerosol Science and Technology*, *51*(5), 543–553. https://doi.org/10.1080/02786826.2017.1280597

Koch, D., & Del Genio, A. D. (2010). Black carbon semi-direct effects on cloud cover: Review and synthesis. *Atmospheric Chemistry and Physics*, *10*(16), 7685–7696. https://doi.org/10.5194/acp-10-7685-2010

Koch, D., Schulz, M., Kinne, S., McNaughton, C., Spackman, J. R., Balkanski, Y., Bauer, S., et al. (2009). Evaluation of black carbon estimations in global aerosol models. *Atmospheric Chemistry and Physics*, *9*(22), 9001–9026. https://doi.org/10.5194/acp-9-9001-2009

Kondo, Y., Ram, K., Takegawa, N., Sahu, L., Morino, Y., Liu, X., & Ohara, T. (2012). Reduction of black carbon aerosols in Tokyo: Comparison of real-time observations with emission estimates. *Atmospheric Environment*, *54*, 242–249. https://doi.org/10.1016/j.atmosenv.2012.02.003

Kristensen, L., Mann, J., Oncley, S. P., & Wyngaard, J. C. (1997). How close is close enough when measuring scalar fluxes with displaced sensors? *Journal of Atmospheric and Oceanic Technology*, *14*(4), 814–821. https://doi.org/10.1175/1520-0426(1997)014<0814:HCICEW>2.0.CO;2

Laborde, M., Mertes, P., Zieger, P., Dommen, J., Baltensperger, U., & Gysel, M. (2012). Sensitivity of the single particle soot photometer to different black carbon types. *Atmospheric Measurement Techniques*, *5*(5), 1031–1043. https://doi.org/10.5194/amt-5-1031-2012

Langford, B., Acton, W., Ammann, C., Valach, A., & Nemitz, E. (2015). Eddy-covariance data with low signal-to-noise ratio: Time-lag determination, uncertainties and limit of detection. *Atmospheric Measurement Techniques*, *8*(10), 4197–4213. https://doi.org/10.5194/amt-8-4197-2015

Lee, L. A., Pringle, K. J., Reddington, C. L., Mann, G. W., Stier, P., Spracklen, D. V., Pierce, J. R., et al. (2013). The magnitude and causes of uncertainty in global model simulations of cloud condensation nuclei. *Atmospheric Chemistry and Physics*, *13*(17), 8879–8914. https://doi.org/10.5194/acp-13-8879-2013

Lee, X., Massman, W., & Law, B. (2005). In X. Lee, W. Massman, & B. Law (Eds.), *Handbook of micrometeorology*, *Atmospheric and Oceanographic Sciences Library*, edited by, (). Netherlands, Dordrecht: Springer.

Lenschow, D. H., & Kristensen, L. (1985). Uncorrelated noise in turbulence measurements. *Journal of Atmospheric and Oceanic Technology*, *2*(1), 68–81. https://doi.org/10.1175/1520-0426(1985)002<0068:UNITM>2.0.CO;2

Liu, J., Fan, S., Horowitz, L. W., & Levy, H. (2011). Evaluation of factors controlling long-range transport of black carbon to the Arctic. *Journal of Geophysical Research*, *116*, D04307. https://doi.org/10.1029/2010JD015145

Mahrt, L. (1998). Flux sampling errors for aircraft and towers. *Journal of Atmospheric and Oceanic Technology*, *15*(2), 416–429. https://doi.org/10.1175/1520-0426(1998)015<0416:FSEFAA>2.0.CO;2

Massman, W. J. (2000). A simple method for estimating frequency response corrections for eddy covariance systems. *Agricultural and Forest Meteorology*, *104*(3), 185–198. https://doi.org/10.1016/S0168-1923(00)00164-7

Menon, S., Koch, D., Beig, G., Sahu, S., Fasullo, J., & Orlikowski, D. (2010). Black carbon aerosols and c. *Atmospheric Chemistry and Physics*, *10*(10), 4559–4571. https://doi.org/10.5194/acp-10-4559-2010

Moncrieff, J., Clement, R., Finnigan, J., & Meyers, T. (2004). Averaging, detrending, and filtering of eddy covariance time series. In *Handbook of micrometeorology*, (pp. 7–31). Dordrecht: Kluwer Academic Publishers.

Moore, C. J. (1986). Frequency response corrections for eddy correlation systems. *Boundary-Layer Meteorology*, *37*(1–2), 17–35. https://doi.org/10.1007/BF00122754

Mori, T., Kondo, Y., Ohata, S., Moteki, N., Matsui, H., Oshima, N., & Iwasaki, A. (2014). Wet deposition of black carbon at a remote site in the East China Sea. *Journal of Geophysical Research: Atmospheres*, *119*, 10485–10498. https://doi.org/10.1002/2014JD022103

Moteki, N., & Kondo, Y. (2010). Dependence of laser-induced incandescence on physical properties of black carbon aerosols: Measurements and theoretical interpretation. *Aerosol Science and Technology*, *44*(8), 663–675. https://doi.org/10.1080/02786826.2010.484450

Nemitz, E., Jimenez, J. L., Huffman, J. A., Ulbrich, I. M., Canagaratna, M. R., Worsnop, D. R., & Guenther, A. B. (2008). An eddy-covariance system for the measurement of surface/atmosphere exchange fluxes of submicron aerosol chemical species—First application above an urban area. *Aerosol Science and Technology*, *42*(8), 636–657. https://doi.org/10.1080/02786820802227352

Nilsson, E. D., Rannik, Ü., Kumala, M., Buzorius, G., & O'dowd, C. D. (2016). Effects of continental boundary layer evolution, convection, turbulence and entrainment, on aerosol formation. *Tellus Series B: Chemical and Physical Meteorology*, *53*(July 2017), 441–461. https://doi.org/10.3402/tellusb.v53i4.16617

Ogren, J. A., Groblicki, P. J., & Charlson, R. J. (1984). Measurement of the removal rate of elemental carbon from the atmosphere. *Science of the Total Environment*, *36*, 329–338. https://doi.org/10.1016/0048-9697(84)90284-5

Ohata, S., Moteki, N., & Kondo, Y. (2011). Evaluation of a method for measurement of the concentration and size distribution of black carbon particles suspended in rainwater. *Aerosol Science and Technology*, *45*(11), 1326–1336. https://doi.org/10.1080/02786826.2011.593590

Ohata, S., Moteki, N., Schwarz, J. P., Fahey, D. W., & Kondo, Y. (2013). Evaluation of a method to measure black carbon particles suspended in rainwater and snow samples. *Aerosol Science and Technology*, *47*(10), 1073–1082. https://doi.org/10.1080/02786826.2013.824067

Papale, D., Reichstein, M., Aubinet, M., Canfora, E., Bernhofer, C., Kutsch, W., Longdoz, B., et al. (2006). Towards a standardized processing of net ecosystem exchange measured with eddy covariance technique: Algorithms and uncertainty estimation. *Biogeosciences*, *3*(4), 571–583. https://doi.org/10.5194/bg-3-571-2006

Petzold, A., Ogren, J. A., Fiebig, M., Laj, P., Li, S. M., Baltensperger, U., Holzer-Popp, T., et al. (2013). Recommendations for reporting black carbon measurements. *Atmospheric Chemistry and Physics*, *13*(16), 8365–8379. https://doi.org/10.5194/acp-13-8365-2013

Pryor, S. C., Barthelmie, R. J., SØrensen, L. L., Larsen, S. E., Sempreviva, A. M., Grönholm, T., Rannik, Ü., et al. (2008). Upward fluxes of particles over forests: When, where, why? *Tellus Series B: Chemical and Physical Meteorology*, *60*(3), 372–380. https://doi.org/10.1111/j.1600-0889.2008.00341.x

Pryor, S. C., Gallagher, M., Sievering, H., Larsen, S. E., Barthelmie, R. J., Birsan, F., Nemitz, E., et al. (2008). A review of measurement and modelling results of particle atmosphere–surface exchange. *Tellus Series B: Chemical and Physical Meteorology*, *60*(1), 42–75. https://doi.org/10.1111/j.1600-0889.2007.00298.x

Pryor, S. C., Larsen, S. E., Sørensen, L. L., & Barthelmie, R. J. (2008). Particle fluxes above forests: Observations, methodological considerations and method comparisons. *Environmental Pollution*, *152*(3), 667–678. https://doi.org/10.1016/j.envpol.2007.06.068

Rannik, Ü., Mammarella, I., Aalto, P., Keronen, P., Vesala, T., & Kulmala, M. (2009). Long-term aerosol particle flux observations part I: Uncertainties and time-average statistics. *Atmospheric Environment*, *43*(21), 3431–3439. https://doi.org/10.1016/j.atmosenv.2009.02.049

Reddy, M. S., & Boucher, O. (2004). A study of the global cycle of carbonaceous aerosols in the LMDZT general circulation model. *Journal of Geophysical Research*, *109*, D14202. https://doi.org/10.1029/2003JD004048

Riley, W. J., Biraud, S. C., Torn, M. S., Fischer, M. L., Billesbach, D. P., & Berry, J. A. (2009). Regional CO_2 and latent heat surface fluxes in the southern Great Plains: Measurements, modeling, and scaling. *Journal of Geophysical Research*, *114*, G04009. https://doi.org/10.1029/2009JG001003

Rowe, M. D., Fairall, C. W., & Perlinger, J. A. (2011). Chemical sensor resolution requirements for near-surface measurements of turbulent fluxes. *Atmospheric Chemistry and Physics*, *11*(11), 5263–5275. https://doi.org/10.5194/acp-11-5263-2011

Ruijrok, W., Davidson, C. I., & Nicholson, K. W. (1995). Dry deposition of particles. *Tellus B*, *47*(5), 587–601. https://doi.org/10.1034/j.1600-0889.47.issue5.6.x

Schwarz, J. P., Doherty, S. J., Li, F., Ruggiero, S. T., Tanner, C. E., Perring, A. E., Gao, R. S., et al. (2012). Assessing single particle soot photometer and integrating sphere/integrating sandwich spectrophotometer measurement techniques for quantifying black carbon concentration in snow. *Atmospheric Measurement Techniques*, *5*(11), 2581–2592. https://doi.org/10.5194/amt-5-2581-2012

Schwarz, J. P., Gao, R. S., Fahey, D. W., Thomson, D. S., Watts, L. A., Wilson, J. C., Reeves, J. M., et al. (2006). Single-particle measurements of midlatitude black carbon and light-scattering aerosols from the boundary layer to the lower stratosphere. *Journal of Geophysical Research*, *111*, D16207. https://doi.org/10.1029/2006JD007076

Sisterson, D. L., Peppler, R. A., Cress, T. S., Lamb, P. J., & Turner, D. D. (2016). The ARM Southern Great Plains (SGP) site. *Meteorological Monographs*, *57*, 6.1–6.14. https://doi.org/10.1175/AMSMONOGRAPHS-D-16-0004.1

Spackman, J. R., Gao, R. S., Neff, W. D., Schwarz, J. P., Watts, L. A., Fahey, D. W., Holloway, J. S., et al. (2010). Aircraft observations of enhancement and depletion of black carbon mass in the springtime Arctic. *Atmospheric Chemistry and Physics*, *10*(19), 9667–9680. https://doi.org/10.5194/acp-10-9667-2010

Spirig, C., Neftel, A., Ammann, C., Dommen, J., Grabmer, W., Thielmann, A., Schaub, A., et al. (2005). Eddy covariance flux measurements of biogenic VOCs during ECHO 2003 using proton transfer reaction mass spectrometry. *Atmospheric Chemistry and Physics*, *5*(2), 465–481. https://doi.org/10.5194/acp-5-465-2005

Stephens, M., Turner, N., & Sandberg, J. (2003). Particle identification by laser-induced incandescence in a solid-state laser cavity. *Applied Optics*, *42*(19), 3726–3736. https://doi.org/10.1364/AO.42.003726

Taipale, R., Ruuskanen, T. M., & Rinne, J. (2010). Lag time determination in DEC measurements with PTR-MS. *Atmospheric Measurement Techniques*, *3*(4), 853–862. https://doi.org/10.5194/amt-3-853-2010

Wesely, M. (1989). Parameterization of surface resistances to gaseous dry deposition in regional-scale numerical models. *Atmospheric Environment*, *23*(6), 1293–1304. https://doi.org/10.1016/0004-6981(89)90153-4

Wienhold, F. (1995). Micrometeorological measurement and source region analysis of nitrous oxide fluxes from an agricultural soil. *Atmospheric Environment*, *29*(17), 2219–2227. https://doi.org/10.1016/1352-2310(95)00165-U

Wilczak, J. M., Oncley, S. P., & Stage, S. A. (2001). Sonic anemometer tilt correction algorithms. *Boundary-Layer Meteorology*, *99*(1), 127–150. https://doi.org/10.1023/A:1018966204465

Wyngaard, J. C. (1973). On surface-layer turbulence. In D. A. Haugen (Ed.), *Workshop on micrometeorology* (392 pp.), Edited by. Boston: American Meteorlogical Society.

Yasunari, T. J., Tan, Q., Lau, K. M., Bonasoni, P., Marinoni, A., Laj, P., Ménégoz, M., et al. (2013). Estimated range of black carbon dry deposition and the related snow albedo reduction over Himalayan glaciers during dry pre-monsoon periods. *Atmospheric Environment*, *78*, 259–267. https://doi.org/10.1016/j.atmosenv.2012.03.031

Zhang, L., Gong, S., Padro, J., & Barrie, L. (2001). A size-segregated particle dry deposition scheme for an atmospheric aerosol module. *Atmospheric Environment*, *35*(3), 549–560. https://doi.org/10.1016/S1352-2310(00)00326-5